ACS Sustainable Chemistry & Engineering

Research Article

pubs.acs.org/journal/ascecg

Facile Synthesis of Well-Dispersed Superparamagnetic γ-Fe_2O_3 Nanoparticles Encapsulated in Three-Dimensional Architectures of Cellulose Aerogels and Their Applications for Cr(VI) Removal from Contaminated Water

Caichao Wan and Jian Li*

Material Science and Engineering College, Northeast Forestry University, Harbin 150040, China

Supporting Information

ABSTRACT: With the increasing emphasis on green chemistry, cellulose aerogels that consist of abundant three-dimensional (3D) architectures have been considered as a class of idea green matrix materials to encapsulate various nanoparticles for synthesis of miscellaneous functional materials. Herein, a facile template synthesis combined with chemical coprecipitation was implemented to prepare hybrid γ-Fe_2O_3@cellulose aerogels (γ-Fe_2O_3@CA). The γ-Fe_2O_3 nanoparticles are well dispersed and immobilized in the micro/nanoscale pore structure of the aerogels, and exhibit superparamagnetic behavior. The particle sizes, pore characteristic parameters, magnetic property, and mechanical strength of the synthetic γ-Fe_2O_3@CA could be flexibly tailored by adjusting the concentrations of the initial reactants. In addition, γ-Fe_2O_3@CA exhibits rapid adsorption rate and excellent adsorption ability to remove Cr(VI) heavy metal ions. Moreover, combined with the advantages of environmental benefits, facile convenient preparation method, high specific surface area and strong mechanical strength, and strong magnetic responsiveness, this class of green γ-Fe_2O_3@CA is more favorable and suitable for Cr(VI) removal from contaminated water, and also useful in many other applications.

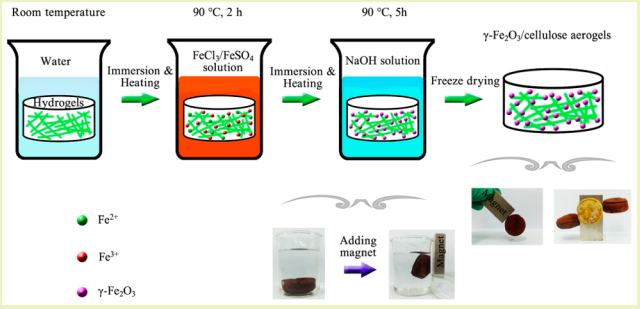

KEYWORDS: *Cellulose aerogels, Superparamagnetic, γ-Fe_2O_3, Composites, Chromium, Adsorption*

INTRODUCTION

Iron oxides in the nano range, have been extensively considered as a fascinating class of materials from the viewpoints of both theory and practical applications, which exhibit tremendous potential in catalytic materials, adsorbents for water purification, gas sensors, ion exchangers, magnetic recording devices, magnetic resonance imaging, bioseparation, etc.[1−5] As one of the most important forms of iron oxides, the cubic spinel structured maghemite (γ-Fe_2O_3) with oxygen atoms forming an fcc close-packed structure, represents nontoxicity, biocompatibility, thermal and chemical stability, favorable hysteric properties, and excellent magnetic properties. In addition, γ-Fe_2O_3 could exhibit unusual superparamagnetic behavior when the particles occur below a critical and material-dependent particle size (the thermal energy exceeds the magnetic anisotropy energy). Besides, superparamagnetic particles do not retain any permanent magnetization after removal of an applied magnetic field, which contributes to their stability and dispersion. Therefore, these characteristics make γ-Fe_2O_3 frequently combined with various matrix materials to fabricate magnetically responsive miscellaneous γ-Fe_2O_3/polymer composites, which usually inherit advantages from both individual components. These polymers include polyacrylate (PEA), polyaniline (PANI), polypyrrole (PPY), polystyrene (PS), poly(3,4-ethylenedioxythiophene) (PEDOT), poly(*N*-isopropylacrylamide) (PNIPAAm), poly(methyl methacrylate) (PMMA), poly(vinyl chloride) (PVC), etc.[6−10]

With the increasing emphasis on green chemistry, it is becoming more important to develop environmentally friendly matrix materials for the synthesis of γ-Fe_2O_3/polymer composites.[11,12] Cellulose aerogels are getting an increasing interest as a class of natural biodegradable template, which consist of cross-linked three-dimensional (3D) architectures formed by self-assembly of cellulose chains as a result of hydrogen-bond interaction. This unique structural feature endows themselves low density, large specific surface area, and high porosity. Indeed, the ordered interior pores of cellulose aerogels are appropriately used as reaction sites, which could provide confined spaces (micro/nanoscale) for insertion of nanoparticles.[13,14] Meanwhile, the strong interactions would occur between abundant surface hydroxyl groups of cellulose and γ-Fe_2O_3 nanoparticles, which are beneficial to immobilization of the particles. The special advantage of this approach is the sharp decline of particle aggregation, and individual,

Received: May 5, 2015
Revised: June 27, 2015
Published: July 23, 2015

DOI: 10.1021/acssuschemeng.5b00384
ACS Sustainable Chem. Eng. 2015, 3, 2142−2152

randomly distributed nanoparticles are formed. Apart from the aforementioned merits, this kind of so-called template-based synthesis method generally has low cost, easily available experimental facilities, and mild technical process, and allows flexibility to design desired morphology, structure and dimension.[15] Therefore, the template-based synthesis method is suitable for fabricating nanomaterials. To date, numerous researches have employed template-based synthesis method to synthesize miscellaneous iron oxides (e.g., α-Fe_2O_3, γ-Fe_2O_3, Fe_3O_4).[16−22] The involved templates include carbon nanotube, hydrochar, ionic liquid [bmim][Cl], iron-based metal organic framework, mesoporous silica, polyethylene glycol (PEG), surfactant micelles (cetyltrimethylammonium bromide), etc. However, the reports using the porous biotemplate (namely cellulose aerogels) to prepare various iron oxides are still rare.[23] Therefore, it might be interesting to synthesize this class of novel biomaterials using cellulose aerogels as template to support magnetic iron oxides, and investigate their potential applications. In addition, cellulose aerogels are generally prepared following the procedures of cellulose dissolution−regeneration−freeze-drying or supercritical drying. Nevertheless, owing to strong inter- and intramolecular hydrogen bonds, high degree of polymerization, and high degree of crystallinity, the raw material (namely cellulose) is difficult to be dissolved or processed in some common water or organic solvents. So far, some effective green cellulose solvents with less harmful effects to people's health and environment have been successively found, such as ionic liquid, *N*-methylmorpholine-*N*-oxide (NMMO), and NaOH/PEG solution.[24−26]

Herein, a facile chemical coprecipitation approach was reported to synthesize the well-dispersed superparamagnetic γ-Fe_2O_3 nanoparticles encapsulated in the 3D architectures of cellulose aerogels. Meanwhile, a green low-cost NaOH/PEG aqueous solution was carried out to fabricate cellulose hydrogels (the precursor of cellulose aerogels), and the waste wheat straw was used as the cellulose source. The nanoparticle sizes, pore characteristic parameters, magnetic properties, and mechanical properties of the synthetic γ-Fe_2O_3@cellulose aerogels (γ-Fe_2O_3@CA) could be flexibly tailored by adjusting the concentrations of the initial reactants. Meanwhile, a possible mechanism schematic for the preparation of the composites is proposed. As an example of potential applications, this class of green γ-Fe_2O_3@CA nanocomposites were used as environmentally friendly adsorbents in heavy metal wastewater treatment (hexavalent chromium, Cr(VI)). In addition, unlike some previous reports[18−20,22] with a final removal treatment of template, the template (i.e., cellulose aerogels) was retained in this paper, considering its numerous good features (e.g., large specific area and pore volume) and importance in the dispersion of nanoparticles that plays an improtant role in adsorption property. Moreover, we expect that the hybrid γ-Fe_2O_3@CA will display a synergistic effect of obtaining a strong ability to adsorb the heavy metal ions.

EXPERIMENTAL SECTION

Materials and Reagents. Native wheat straw was grinded and then screened through a 60-mesh sieve, and the resulting powder was subsequently collected and dried in a vacuum oven at 60 °C for 24 h before used. All chemical reagents with analytical grade were purchased from Tianjin Kemiou Chemical Reagent Co., Ltd. (China) and used without further purification.

Preparation of Hybrid γ-Fe_2O_3@CA. The isolation of cellulose from native wheat straw was carried out by a facile chemical treatment method, which could refer to our previous report.[27] The obtained dried cellulose (1.0 g) was mixed with the 10% aqueous solution of NaOH/PEG-4000 (9:1 wt/wt) with magnetic stirring for 5 h at room temperature to form a 2 wt % homogeneous cellulose solution. Then, the cellulose solutions was frozen at −15 °C for 12 h, and subsequently thawed at room temperature under vigorous stirring for 30 min. After being frozen at −15 °C for 5 h again, the frozen cake was immediately immersed in a 1% HCl solution for 6 h, and this immersion process was repeated several times until the formation of a cylindrical hydrogel. After being repeatedly rinsed with distilled water for the removal of excess hydrogen ions, the cellulose hydrogel was immersed in a freshly prepared aqueous solution of $FeCl_3$ and $FeSO_4$ (50 mL) with a constant molar ratio of $[Fe^{3+}]/[Fe^{2+}] = 2$, and the mixture was subsequently heated to 90 °C and held at this temperature for 2 h. After that, the hydrogel was placed into a NaOH solution (2 mol·L^{-1}, 60 mL), and the color of the sample immediately changed from orange/green to black as inorganic nanoparticles formed in the hydrogel matrix. Thereafter, the system was kept for an additional 5 h at 90 °C. Note that all reactions were performed in air. Finally, the resulting product was washed thoroughly to remove residual chemicals, and subsequently underwent a *tert*-butyl alcohol freeze-drying treatment at −35 °C for 24 h, and the following hybrid γ-Fe_2O_3@CA was generated. In addition, the pure cellulose aerogels (PCA) were prepared by the direct *tert*-butyl alcohol freeze-drying treatment of the cellulose hydrogels without the aforementioned heating and immersion processes.

Characterization Techniques. Transmission electron microscopy (TEM) and high-resolution TEM (HRTEM) observations, and selected area electron diffraction (SAED) were performed with a FEI, Tecnai G2 F20 TEM with a field-emission gun operating at 200 kV. The samples were suspended in ethanol and were prepared by being drop-cast onto a carbon-coated 200-mesh copper grid and subsequently dried at room temperature.

N_2 adsorption−desorption measurements were implemented at −196 °C using an accelerated surface area and porosimetry system (3H-2000PS2 unit, Beishide Instrument S&T Co., Ltd.). Prior to the measurements, all of the samples were outgassed at 90 °C for 10 h for the removal of any moisture or adsorbed contaminants. The specific surface area was calculated over a relative pressure range of 0.05−0.30 from the multipoint Brunauer−Emmett−Teller (BET) method. The nitrogen adsorption volume at the relative pressure (P/P_0) of 0.994 was used to determine the pore volume. The pore diameter distributions were calculated from the data of the adsorption branch of the isotherm using the Barrett−Joyner−Halenda (BJH) method.

X-ray photoelectron spectroscopy (XPS) was carried out using a Thermo Escalab 250Xi XPS spectrometer equipped with a dual X-ray source using Al Kα. Deconvolution of the overlapping peaks was performed using a mixed Gaussian−Lorentzian fitting program (Origin 8.5, Originlab Corporation). X-ray diffraction (XRD) spectroscopy was implemented on a Bruker D8 Advance TXS XRD instrument with Cu Kα (target) radiation (λ = 1.5418 Å) at a scan rate (2θ) of 4°·min^{-1} and a scan range from 5° to 90°. Fourier transform infrared spectra (FTIR) were recorded by a Nicolet Nexus 670 FTIR instrument in the range of 400−4000 cm^{-1} with a resolution of 4 cm^{-1}. All of the samples were ground into a powder and then blended with KBr before pressing the mixture into ultrathin pellets. Thermal stabilities were determined using a thermal gravity (TG) analyzer (TA, Q600) from room temperature to 800 °C at a heating rate of 10 °C·min^{-1} under a nitrogen atmosphere. A Quantum Design Magnetometer (MPMS XL-7) using a superconducting quantum interference device (SQUID) sensor was used to make measurements of the magnetic properties of the composites in applied magnetic fields over the range from −20 000 to +20 000 Oe at 298 K.

Compression tests were performed with a universal testing machine (Suns, UTM4304X), and the compressing velocity was set to 2 mm·min^{-1}. Before the tests, the aerogels were tailored to the same sizes of around 30 mm in diameter and 10 mm in length. The modulus was calculated from the initial linear region of the stress−strain curves in low strain (<6%). The energy absorption by the samples was taken as the area below the stress−strain curve between 0% and 90% strain.

DOI: 10.1021/acssuschemeng.5b00384
ACS Sustainable Chem. Eng. 2015, 3, 2142−2152

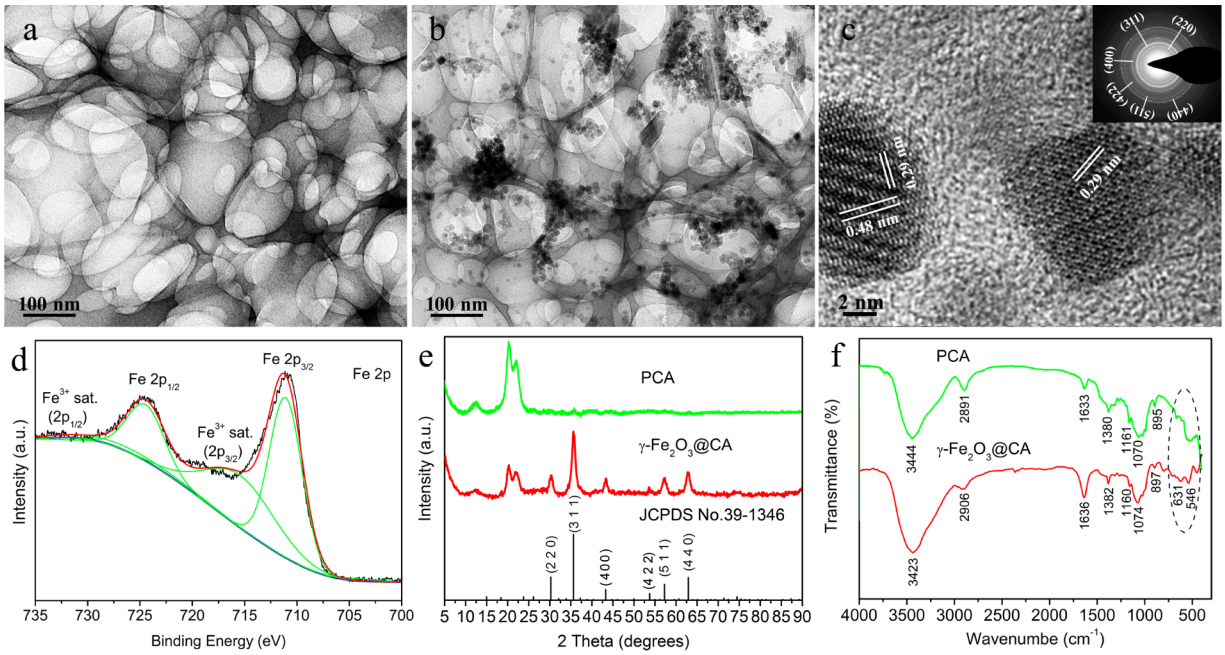

Figure 1. (a) TEM image of PCA. (b) TEM image, (c) HRTEM image, and (d) XPS spectrum of γ-Fe_2O_3@CA. The inset in panel c shows the SAED pattern of γ-Fe_2O_3@CA. (e) XRD patterns of PCA and γ-Fe_2O_3@CA, respectively. The positions and intensities of the diffraction lines of γ-Fe_2O_3 (i.e., JCPDS No. 39-1346) are shown at the bottom. (f) FTIR spectra of PCA and γ-Fe_2O_3@CA, respectively.

Cr(VI) Adsorption Experiments. Solutions with different concentrations of Cr(VI) were prepared using $K_2Cr_2O_7$ as the source of heavy metal ions, respectively. The pH value was adjusted to 3 using HCl (0.1 M). The as-prepared PCA and γ-Fe_2O_3@CA were used as adsorbents. For the adsorption kinetic study, 100 mg of adsorbent was added to 50 mL solutions with a Cr(VI) initial concentration of 10 $mg{\cdot}L^{-1}$. After a specified time, the adsorbent was separated by centrifugation from the Cr(VI) solutions, and the supernatant was collected and analyzed using an inductively coupled plasma−mass spectrometer (ICP-MS; Agilent 7700, Agilent Technologies, Santa Clara, California) to measure the concentration of Cr(VI) in the remaining solution. For the adsorption isothermal study, 50 mg of adsorbent was added to 25 mL of solution with different concentrations under stirring for 2 h at room temperature. After the centrifugal separation, the concentration of Cr(VI) in the supernatant was also tested. Note that all the adsorption experiments were carried out at room temperature.

RESULTS AND DISCUSSION

Characterizations of γ-Fe_2O_3@CA by TEM, SAED, XPS, XRD, and FTIR. Micro/nanoscale 3D architectures of the aerogels are suitable reacting sites, which allow guest molecules to penetrate into their inner spaces (Figure 1a). Meanwhile, strong electrostatic interactions would occur between the incorporated Fe^{2+}/Fe^{3+} ions and cellulose macromolecules, on account that the electron-rich oxygen atoms of polar hydroxyl and ether groups of cellulose are expected to interact with the electropositive transition metal cations. This interaction would result in the immobilization of cations in the aerogels matrix, contributing to uniform distribution and stability.[28−30] The subsequent dipping process accompanied by heating results in the transformation of cations and the ultimate in situ formation of γ-Fe_2O_3 nanoparticles, and the nanoparticles are stabilized at the previous ionized selective sites of the cellulose surface without drastic aggregation as shown in Figure 1b.

The HRTEM image of γ-Fe_2O_3@CA reveals the presence of γ-Fe_2O_3 as shown in Figure 1c; i.e., lattice fringes with spacings of around 0.48 and 0.29 nm agree well with the (111) and (220) lattice spacings.[31] Besides, the corresponding SAED pattern exhibits homogeneous ring patterns typical of nanocrystalline materials, and is consistent with the lattice spacing of cubic γ-Fe_2O_3 (the inset in Figure 1c). XPS was used to precisely determine the oxidation state of the synthesized particles. The Fe 2p peaks at binding energies of 711.2 and 724.7 eV (Figure 1d), closely correspond to the Fe $2p_{3/2}$ and Fe $2p_{1/2}$ spin−orbit peaks of γ-Fe_2O_3.[32] The satellite peak at around 719.3 eV is another evidence of Fe^{3+}. For further clarifying the crystal structure and phase purity of the synthesized particles, XRD analysis was carried out. For comparison, the XRD patterns were both normalized to the maximum line intensity. As shown in Figure 1e, the cellulose characteristic peaks could be seen at around 12.3°, 20.2°, and 22.0° for both PCA and γ-Fe_2O_3@CA, corresponding to (101), (10$\bar{1}$), and (002) planes. Besides, the peaks of γ-Fe_2O_3@CA at around 30.2°, 35.6°, 43.4°, 53.7°, 57.4°, and 62.9° are consistent with the JCPDS file of γ-Fe_2O_3 (No. 39-1346). Moreover, the *d*-spacings also match well with the JCPDS file (see Table S1 and Figure S1), indicating the formation of γ-Fe_2O_3 with a cubic spinel crystalline structure. Meanwhile, there is no indication of any other iron oxide phases in the XRD pattern of γ-Fe_2O_3@CA. Figure 1f presents the FTIR spectra of PCA and γ-Fe_2O_3@CA. Apart from the characteristic peaks derived from cellulose (for details, see the Supporting Information), the FTIR spectrum of γ-Fe_2O_3@CA presents two new peaks located at 546 and 634 cm^{-1} related to stretching vibration of Fe−O (Figure 1f),[33] which further prove the generation of γ-Fe_2O_3. Meanwhile, the band at 3039−3710 cm^{-1} assigned to the stretching vibrations of hydroxyl groups, shifts from 3444 cm^{-1} to the lower wavenumber 3423 cm^{-1}, suggesting the strong interaction between the hydroxyl groups of cellulose aerogels and the encapsulated γ-Fe_2O_3. From the above, the γ-Fe_2O_3 nanoparticles were successfully fabricated and encapsulated in the 3D architectures of cellulose aerogels with good dispersion via the aforementioned facile approach.

DOI: 10.1021/acssuschemeng.5b00384
ACS Sustainable Chem. Eng. 2015, 3, 2142−2152

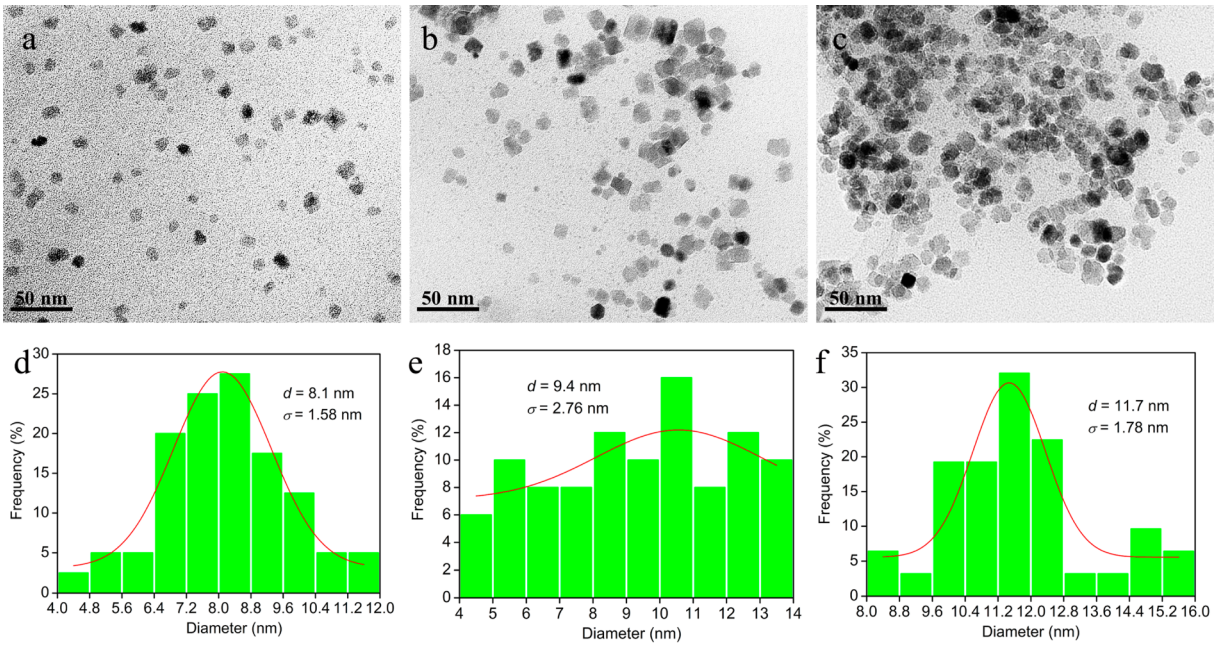

Figure 2. TEM images of (a) γ-Fe_2O_3@CA-001, (b) γ-Fe_2O_3@CA-005, and (c) γ-Fe_2O_3@CA-01. (d, e, and f) are the corresponding particle diameter distributions of the composites of (a, b, and c).

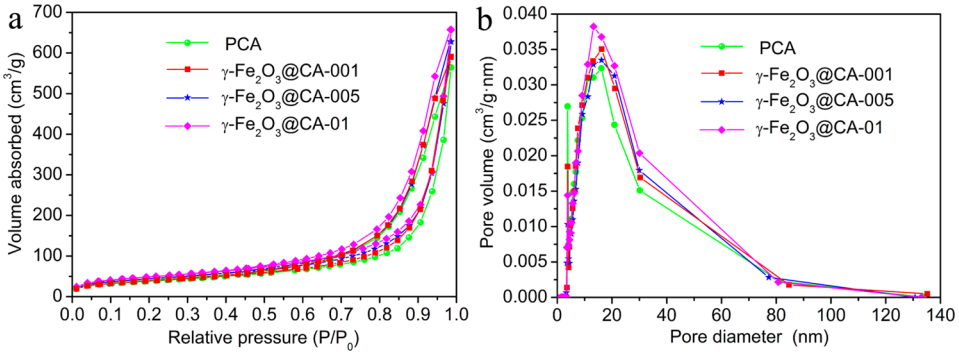

Figure 3. (a) N_2 adsorption−desorption isotherms and (b) pore size distributions of PCA, γ-Fe_2O_3@CA-001, γ-Fe_2O_3@CA-005, and γ-Fe_2O_3@CA-01, respectively.

Tunability of γ-Fe_2O_3 Nanoparticles Sizes by Concentrations of Initial Reactants. The sizes of nanoparticles could be tailored by altering the total concentration of the $FeCl_3/FeSO_4$ salts (with a fixed molar ratio of 2) from 0.01 to 0.05 mol·L^{-1} and 0.1 mol·L^{-1}, and the resulting composites are marked as γ-Fe_2O_3@CA-001, γ-Fe_2O_3@CA-005, and γ-Fe_2O_3@CA-01, respectively. As shown in Figure 2a−c, the faceted shaped nanoparticles exhibit favorable dispersion, whereas their sizes are obviously varied with the concentrations of initial reactants. Their size distributions are presented in Figure 2d,e. It could be seen that the average size (d) increases from 8.1 to 9.4 nm and eventually to 11.7 nm when the concentration of ferrous ions gradually increases from 0.01 to 0.05 mol·L^{-1} and eventually to 0.1 mol·L^{-1}. This upward tendency could be ascribed to the nucleation stage of the nanoparticles. When the concentration of consistent species reaches the supersaturation, a nucleation stage would occur; i.e., the nuclei starts to grow by flocculation or aggregation of nuclei into larger particles until the aforementioned final size is obtained. Therefore, the increase of reactant concentration produces positive effect to reach the sufficient number of nanoparticles for the nucleation and growth stages. Besides, the formed greater number of small crystals are prone to aggregation owing to the strong interaction and high reactant concentration, which results in higher sizes. Meanwhile, in the accompanying Ostwald ripening, small crystals would shrink while large ones would grow, then lead to a broad size distribution.[34]

Pore Structure Characteristics, and Thermal, Mechanical and Magnetic Properties of γ-Fe_2O_3@CA. N_2 adsorption−desorption isotherms provide much useful information about the pore structures of this class of hybrid γ-Fe_2O_3@CA (Figure 3a). These isotherms could all be classified to type IV according to IUPAC classification,[35] and the adsorption−desorption loops belong to the type H3,[36] which reveals the existence of slit-shaped pores. The adsorption uptakes in the P/P_0 range between 0 and 0.6 increase slightly for all the samples, indicating the existence of few micropores. Meanwhile, nitrogen molecules are gradually adsorbed on the internal surface of porous structures from single to multilayer in this period. Thereafter, the adsorption amounts increase quickly in the range of 0.6−1, which generates obvious hysteresis loops, and still do not reach a plateau near the P/P_0 of 1.0, revealing the presence of mesopores and macropores. The results are in good agreement with the observation from TEM images.

DOI: 10.1021/acssuschemeng.5b00384
ACS Sustainable Chem. Eng. 2015, 3, 2142−2152

Table 1. Characteristics of PCA and γ-Fe_2O_3@CA with the Different Precursor Concentrations

sample	γ-Fe_2O_3 fraction (wt %)	particle size (nm)	specific surface area (m^2/g)	pore volume (cm^3/g)	elasticity modulus (MPa)	energy absorption (kJ/m^3)	saturation magnetization (emu/g)
PCA			136.8	0.88	1.58	240.8	
γ-Fe_2O_3 @CA-001	14.1	8.1 ± 1.58	140.8	0.92	2.09	338.9	1.6
γ-Fe_2O_3 @CA-005	26.2	9.4 ± 2.76	156.3	0.97	2.68	487.8	9.9
γ-Fe_2O_3 @CA-01	34.1	11.7 ± 1.78	173.5	1.02	3.19	658.0	18.0

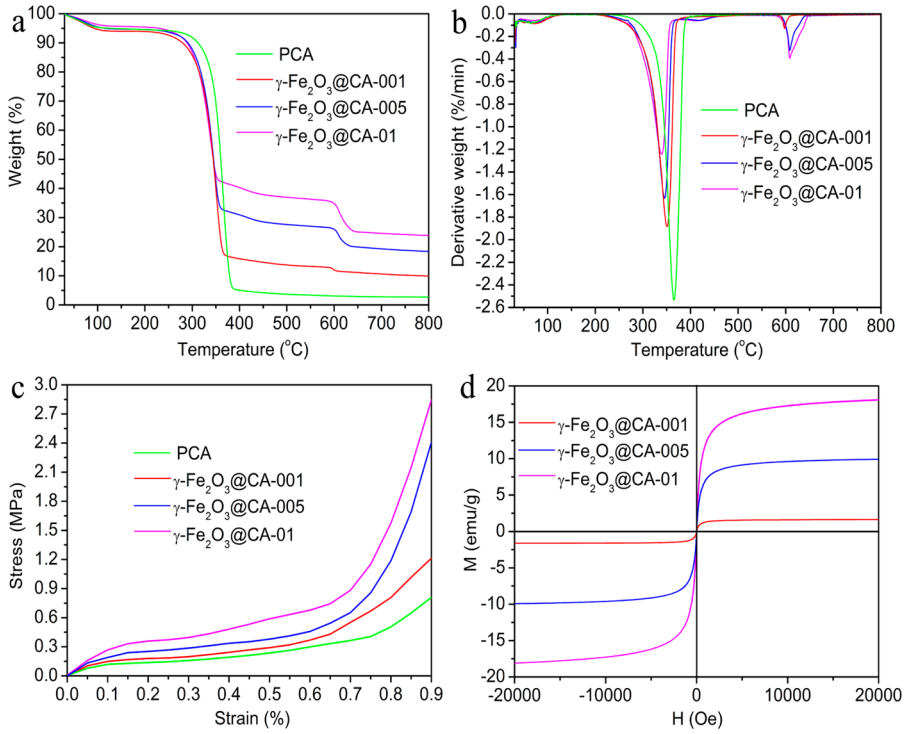

Figure 4. (a) TG curves, (b) DTG curves, and (c) compression stress−strain curves of PCA, γ-Fe_2O_3@CA-001, γ-Fe_2O_3@CA-005, and γ-Fe_2O_3@CA-01, respectively. (d) Hysteresis cycles of γ-Fe_2O_3@CA-001, γ-Fe_2O_3@CA-005, and γ-Fe_2O_3@CA-01.

Moreover, the pore size distributions as shown in Figure 3b also prove the existence of mesopores and macropores, which exhibit that the pore sizes are within the scope of 3−140 nm. Besides, the two maximum peaks at around 3.8 and 16.1 nm could also be clearly distinguished. BET and BJH analysis gives specific surface areas and pore volumes of 136.8 m^2/g and 0.88 cm^3/g for PCA, 140.8 m^2/g and 0.92 cm^3/g for γ-Fe_2O_3@CA-001, 156.3 m^2/g and 0.97 cm^3/g for γ-Fe_2O_3@CA-005, and 173.5 m^2/g and 1.02 cm^3/g for γ-Fe_2O_3@CA-01, as shown in Table 1, respectively. It could be seen that the insertion of γ-Fe_2O_3 improves the pore characteristic parameters of the composites compared with those of PCA. Besides, the specific surface area and pore volume of the composites are effectively controlled by the content of incorporated γ-Fe_2O_3 nanoparticles. The values apparently increase with the increasing of the γ-Fe_2O_3 nanoparticles content. These enhancement phenomena might be on account that the insertion of higher content of nanoparticles more effectively strengthens the 3D skeleton structure of the aerogels, leading to more resistant to shrinkage and collapse during the drying treatment.

Considering the importance of thermal stability in the applications of nanocomposites, the thermal behaviors of the synthetic composites and PCA were studied by TG technique. TG and derivative thermal gravity (DTG) traces of these materials exhibit three major weight loss peaks at around 40−120, 217−400, and 585−648 °C (Figure 4a,b). The two former peaks are attributed to the evaporation of absorbed water and the decomposition of cellulose,[37] respectively. Moreover, for the investigation of the weight loss at 585−648 °C, γ-Fe_2O_3@CA-01 was selected as an example to undergo the thermal treatments at various temperatures (the details about the processes are given in the Supporting Information), and the resulting products were tested by XRD to identify the compositions. As shown in Figure S2, after the thermal treatment at 610 °C, γ-Fe_2O_3@CA-01 is reduced to Fe (JCPDS No. 65-4899, denoted with triangles) possibly due to the reaction occurring between the γ-Fe_2O_3 nanoparticles and the residual char obtained from the pyrolysis of cellulose. Meanwhile, this reaction also results in the oxidation of residual char to carbon dioxide, leading to weakening or disappearance of graphite characteristic peaks of residual char. Therefore, the reaction between the γ-Fe_2O_3 and the residual char is responsible for this weight loss. As the processing temperature rises from 610 to 660 °C and eventually to 800 °C, the XRD peaks of γ-Fe_2O_3 gradually weaken and disappear, whereas the new peaks corresponding to $CFe_{15.1}$ (JCPDS No. 52-0512) are generated at 800 °C. In addition, regardless of the impurities with low content (i.e., $CFe_{15.1}$ and carbon residue),

DOI: 10.1021/acssuschemeng.5b00384
ACS Sustainable Chem. Eng. 2015, 3, 2142−2152

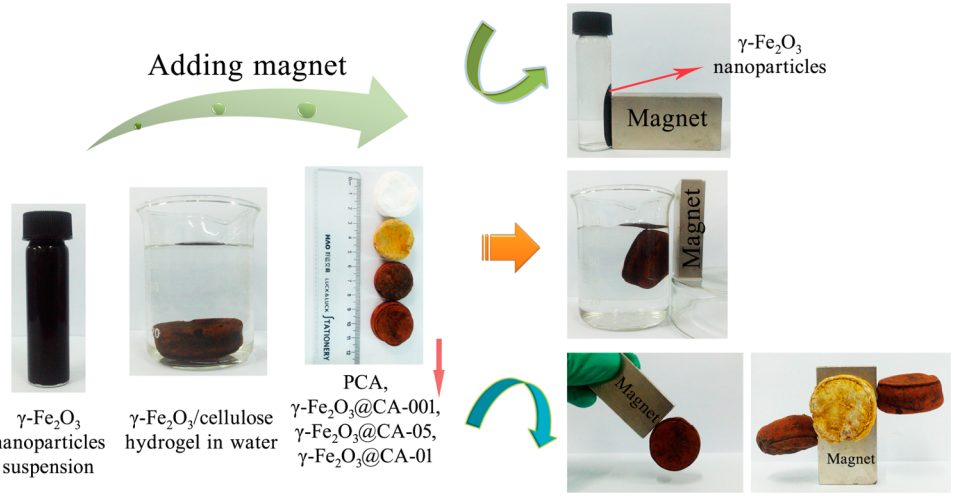

Figure 5. Magnetic responsiveness of γ-Fe_2O_3 nanoparticles, γ-Fe_2O_3@cellulose hydrogels, and γ-Fe_2O_3@CA.

we suppose that the products at 800 °C only consist of Fe. Thus, the contents of γ-Fe_2O_3 could be roughly calculated to be 14.1% in γ-Fe_2O_3@CA-001, 26.2% in γ-Fe_2O_3@CA-005, and 34.1% in γ-Fe_2O_3@CA-01, respectively.

In addition, the well-known inferior mechanical properties of this class of porous aerogels, which result from the defects such as dangling ends and loops in their structures,[38] are the main challenges that require urgent attention and immediate improvement. However, the combination with various fillers such as $CoFe_2O_4$, clay, graphene oxide, silica, and polypyrrole has been reported to contribute to improving significantly the mechanical properties and fragility of aerogels.[39−43] Therefore, we expect that the incorporation of γ-Fe_2O_3 will also be helpful to enhance the mechanical strength of the hybrid aerogels. The stress−strain behaviors were measured to determine and compare the mechanical properties of PCA and γ-Fe_2O_3@CA. As shown in Figure 4c, the compression stress−strain curve could be roughly divided into four stages.[44] First, the linear elastic behavior resulted from elastic cell wall bending takes place in low strain (<6%); second, the curves gradually transform from linear to nonlinear in higher strain; third, a horizontal plateau region appears after reaching yield stress, and cell collapse typically occurs; final, the loose porous 3D network structure starts to touch, resulting in considerable stiffening. The composites have higher compressibility than that of PCA. The elasticity modulus value of PCA is 1.58 MPa, and the value increase from 2.09 MPa for γ-Fe_2O_3@CA-001 to 2.68 MPa for γ-Fe_2O_3@CA-005 and eventually to 3.19 MPa for γ-Fe_2O_3@CA-01. Moreover, the energy absorption in compression is calculated to be 240.8 $kJ{\cdot}m^{-3}$ for PCA, 338.9 $kJ{\cdot}m^{-3}$ for γ-Fe_2O_3@CA-001, 487.8 $kJ{\cdot}m^{-3}$ for γ-Fe_2O_3@CA-005, and 658.0 $kJ{\cdot}m^{-3}$ for γ-Fe_2O_3@CA-01. The higher values reveal the stronger resistance to compression deformation. These results indicate that the incorporation of γ-Fe_2O_3 nanoparticles contributes to apparent improvement in the compression mechanical properties of the composites. Meanwhile, the higher particles loading contents possibly induce further enhancement in the mechanical properties from γ-Fe_2O_3@CA-001 to γ-Fe_2O_3@CA-01.

The room-temperature hysteresis cycles of the composites show absence of hysteresis and coercivity (Figure 4d), which is characteristic of superparamagnetic behavior caused by the small particle size of γ-Fe_2O_3 smaller than the related critical single-domain size.[45] The curves all increase rapidly with increasing applied magnetic field, which exhibit saturation magnetization (M_s) values of 1.6 emu/g for γ-Fe_2O_3@CA-001, 9.9 emu/g for γ-Fe_2O_3@CA-005, and 18.0 for γ-Fe_2O_3@CA-01. Apparently, the M_s values significantly increase as the total concentration of the $FeCl_3/FeSO_4$ salts increases, which demonstrates the tailorability of the magnetic property. Additionally, taking the nanoparticles contents in the samples (14.1%, 26.2%, and 34.1%) into consideration, the corresponding calculated M_s values are 11.3, 37.8, and 52.8 emu/g, which are much smaller than the theoretical M_s of 76 emu/g for bulk γ-Fe_2O_3. The above differences might be explained by the small particle size effect.[46] In detail, bulk γ-Fe_2O_3 has a spinel-type collinear ferrimagnetic spin structure. Noncollinear spin arrangement at or near the surface of the particle due to a surface effect, is more pronounced in small particle sizes, which significantly affects the magnetic properties. Meanwhile, the cation disorder and magnetically disordered surface layer around the particles could also be responsible for the lower saturation magnetization. Besides, the presence of amorphous impurities (e.g., carbon residue) and carbide impurities (e.g., $CFe_{15.1}$) also can reduce the total magnetization. Additionally, these magnetic materials reach the saturation magnetization at relatively low applied fields (ca. 5 kOe), which might be useful in some special occasions, where a strong magnetic signal is required at small applied magnetic fields (e.g., magnatic resonance imaging, magnetic separation, drug delivery, etc.).[47]

Macroscopic Phenomena of Magnetic Responsiveness of γ-Fe_2O_3 Nanoparticles, γ-Fe_2O_3@Cellulose Hydrogels, and γ-Fe_2O_3@CA. The synthetic γ-Fe_2O_3 nanoparticles and the related hybrid products including hydrogels and aerogels are demonstrated to be magnetically responsive materials and actuators as shown in Figure 5. It could be seen that the nanoparticles could be easily recycled from the black suspension by magnet attraction (see also Supplementary Video 1). The hydrogels are sensitive to the applied magnetic field, which could flexibly float in the water following the magnet movement (see also Supplementary Video 2). In addition, the dried aerogels from the different reactants concentrations (γ-Fe_2O_3@CA-001, -005, and -01) also exhibit favorable magnetic responsiveness. They could tightly adhere to the magnet surface, and maintain well-defined shapes (see also Supplementary Video 3). Therefore, this class of magnetically

DOI: 10.1021/acssuschemeng.5b00384
ACS Sustainable Chem. Eng. 2015, 3, 2142−2152

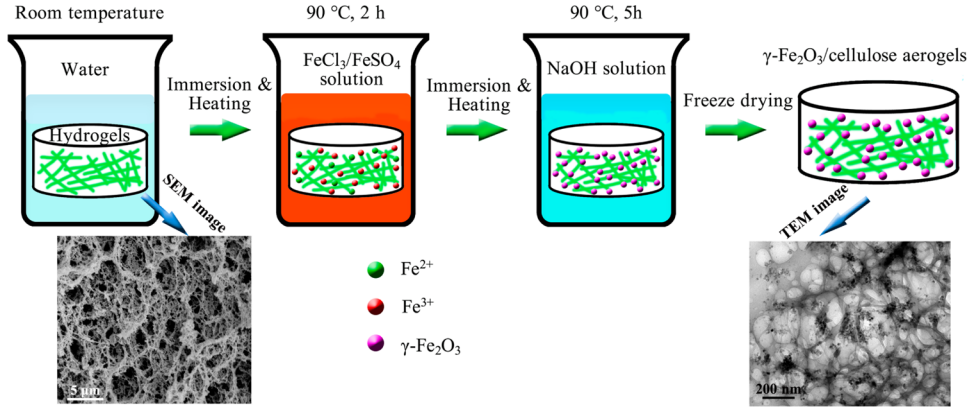

Figure 6. Schematic illustration for the preparation of γ-Fe_2O_3@CA.

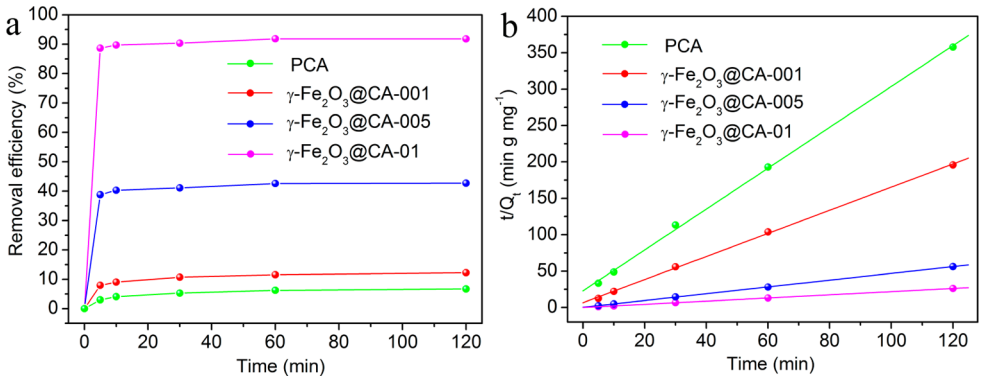

Figure 7. (a) Adsorption kinetics of Cr(VI) and (b) pseudo-second-order model for adsorption of Cr(VI) on PCA, γ-Fe_2O_3@CA-001, γ-Fe_2O_3@CA-005, and γ-Fe_2O_3@CA-01, respectively.

responsive aerogels with high mechanical strength and large specific surface might find some potential applications like recyclable green magnetically driven adsorbents for water purification, and some biodegradable electromagnetic devices.

Schematic Illustration for Preparation of γ-Fe_2O_3@CA. The schematic illustration for the preparation of γ-Fe_2O_3@CA is presented in Figure 6. As previously mentioned, the metal ions are tightly anchored to the surface of cellulose chains by strong electrostatic (i.e., ion−dipole) interactions. The subsequent immersion in NaOH solution leads to the formation of γ-Fe_2O_3 nanoparticles, which are stabilized at the previous ionized selective sites resulting in a good dispersion. Moreover, the drying method (i.e., freeze-drying) causes limited shrinkage, which contributes to maintaining the original 3D skeleton structure of the hydrogels. The insertion of γ-Fe_2O_3 further strengthens the 3D skeleton, and enhances resistance to shrinkage and collapse.[48]

Heavy Metal Ion Cr(VI) Adsorption Properties of γ-Fe_2O_3@CA. For the investigation of the potential applications of γ-Fe_2O_3@CA, we used this class of nanocomposites as environmentally friendly adsorbents in heavy metal wastewater treatment. Cr(VI) is a common heavy metal contaminant in water resources, which has been designated as one of the top-priority toxic pollutants by the U.S. EPA due to its carcinogenesis and strong toxicity to humans and animals. Cr(VI) is usually released from various industrial operations, such as chromate production, mining and metallurgy, petroleum refining, electroplating, leather tanning, etc.[49] Unreasonably treated or even untreated Cr(VI)-containing wastewater is arbitrarily discharged, resulting in the serious Cr(VI) contamination. Undoubtedly, effective removal of Cr(VI) from water is of great significance. So far, all sorts of adsorbents including natural materials (e.g., clay, rice husk ash, activated alumina, fuller's earth, fly ash, saw dust) and synthetic materials (e.g., active carbon, mesoporous silica, polyaniline coated ethyl cellulose) have been carried out to treat with Cr(VI)-containing wastewater.[50−54] However, compared with these adsorbents, γ-Fe_2O_3@CA has not only good environmental benefits and strong selectiveness in Cr(VI) removal,[55] but also excellent magnetic responsibility contributing to achieving a given level of magnetic separation with much less energy. Besides, due to the large specific surface area and 3D hierarchical porous structure of the aerogels template as well as good dispersion of nanoparticles, we expect that the hybrid γ-Fe_2O_3@CA will display a synergistic effect of obtaining a strong ability to adsorb Cr(VI).

The adsorption kinetics of Cr(VI) on PCA, γ-Fe_2O_3@CA-001, γ-Fe_2O_3@CA-005, and γ-Fe_2O_3@CA-01 are presented in Figure 7a. Interestingly, the four kinds of materials all have rapid Cr(VI) adsorption capacity, and reach adsorption equilibrium within several minutes. Moreover, γ-Fe_2O_3@CA-01 displays the Cr(IV) removal efficiency of 91.8%, much higher than those of γ-Fe_2O_3@CA-005 (42.7%), γ-Fe_2O_3@CA-001 (12.3%), and PCA (6.7%) under the same conditions, indicating the potential stronger adsorption property for Cr(VI) removal. In Figure 7b, the adsorption kinetics data is well fitted by the pseudo-second-order rate kinetic model expressed as eq 1.[56]

DOI: 10.1021/acssuschemeng.5b00384
ACS Sustainable Chem. Eng. 2015, 3, 2142−2152

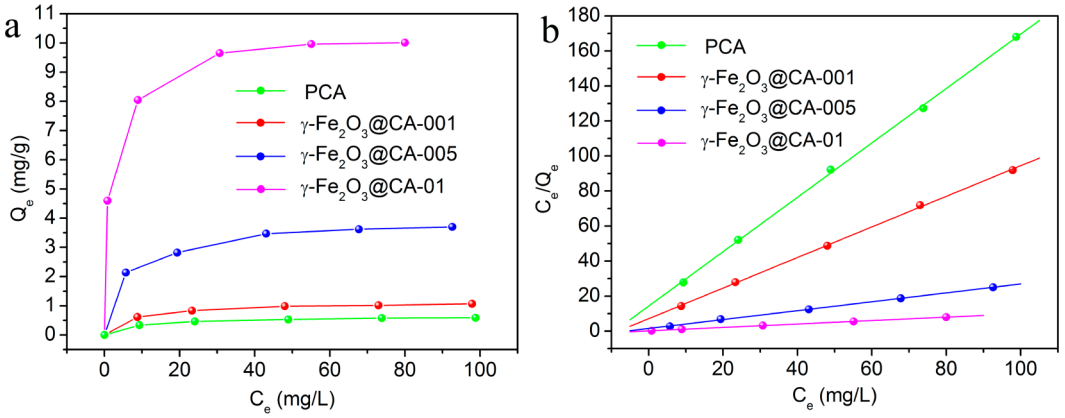

Figure 8. (a) Adsorption isotherms of Cr(VI) and (b) Langmuir isotherms plots of Cr(VI) adsorption on PCA, γ-Fe_2O_3@CA-001, γ-Fe_2O_3@CA-005, and γ-Fe_2O_3@CA-01, respectively.

$$\frac{t}{Q_t} = \frac{t}{Q_e} + \frac{1}{K_2 Q_e^{\,2}} \quad (1)$$

where Q_e and Q_t ($mg \cdot g^{-1}$) is the amount of adsorbed heavy metal at equilibrium and at time t, respectively. K_2 is the adsorption rate constant ($g \cdot mg^{-1} \cdot min^{-1}$). The correlation coefficients (R^2) for PCA, γ-Fe_2O_3@CA-001, γ-Fe_2O_3@CA-005, and γ-Fe_2O_3@CA-01 are 0.9988, 0.9992, 0.9999, and 0.9999, indicating that the Cr(VI) adsorption follows the pseudo-second-order kinetic model. According to the slope and intercept, the K_2 values are calculated to be 0.3433, 0.3800, 0.6035, and 0.7364 $g \cdot mg^{-1} \cdot min^{-1}$ for PCA, γ-Fe_2O_3@CA-001, γ-Fe_2O_3@CA-005, and γ-Fe_2O_3@CA-01, respectively. Apparently, the K_2 values increase with the increase of γ-Fe_2O_3 content, which reveals that the higher γ-Fe_2O_3 proportion contributes to the improvement in Cr(VI) adsorption rate.

Additionally, the adsorption mechanisms of γ-Fe_2O_3@CA for Cr(VI) is postulated to primarily involve electrostatic attraction.[55,57] It has been proposed that cellulose and iron oxide surfaces are protonated at low pH, so that the surface charge is positive. Meanwhile, when the pH value is lower than 6.8, $HCrO_4^-$ is the dominant form of hexavalent chromium in solution. Therefore, the strong electrostatic attraction would occur between the positively charged γ-Fe_2O_3@CA and the negatively charged Cr(VI) ($HCrO_4^-$) species, allowing the approach of the Cr(VI) ions to the adsorbent surfaces. Moreover, the above phenomenon (i.e., the positive correlation between the γ-Fe_2O_3 proportion and the Cr(VI) adsorption rate) is possibly attributed to more adsorption sites on the surface of the absorbent when γ-Fe_2O_3@CA with higher γ-Fe_2O_3 proportion was used.

Figure 8a shows the adsorption isotherms of Cr(VI) on PCA, γ-Fe_2O_3@CA-001, γ-Fe_2O_3@CA-005, and γ-Fe_2O_3@CA-01, which are obtained with different initial concentrations ranging from 10 to 100 $mg \cdot L^{-1}$. Apparently, for all the samples, the isotherms rapidly increase in the lower concentration region, and subsequently gradually flatten out in the high concentration region. The Langmuir adsorption model is adopted to fit the equilibrium adsorption data and estimate the maximum adsorption capacity. The linearized form of the Langmuir equation isotherm is expressed as eq 2:[58]

$$\frac{C_e}{Q_e} = \frac{1}{K_L Q_m} + \frac{C_e}{Q_m} \quad (2)$$

where Q_e is the amount of Cr(VI) adsorbed per unit weight of the adsorbent at equilibrium (mg/g), C_e is the equilibrium concentration of Cr(VI) (mg/L), K_L is the Langmuir adsorption equilibrium constant related to the energy, and Q_m is the maximum adsorption capacity (mg/g). As shown in Figure 8b, the experimental data fits the Langmuir adsorption model well, with R^2 of 0.9992 for PCA, 0.9993 for γ-Fe_2O_3@CA-001, 0.9989 for γ-Fe_2O_3@CA-005, and 0.9997 for γ-Fe_2O_3@CA-01. In addition, the maximum adsorption capacities (Q_m) of these samples calculated from the Langmuir isotherm model are listed in Table 2. For comparison, some literature values of Q_m of other iron-oxide-based adsorbents for Cr(VI) adsorption are also given.[59−63] Among the four kinds of adsorbents in this study, PCA has the lowest Q_m of 0.64 mg/g. The similar phenomenon also has been observed by Dupont and Guillon.[64] They conducted studies on Cr(VI) adsorption with pure cellulose at acidic pH, and the results also display no significant adsorption onto cellulose. However, the Q_m of PCA is still close to that of commercial α-Fe_2O_3 (0.68 mg/g). With the incorporation of γ-Fe_2O_3, the Q_m values significantly increase from 1.14 mg/g for γ-Fe_2O_3@CA-001 to 3.94 mg/g for γ-Fe_2O_3@CA-005 and eventually to 10.2 mg/g for γ-

Table 2. Comparison of Maximum Adsorption Capacities of PCA, γ-Fe_2O_3@CA-001, γ-Fe_2O_3@CA-005, and γ-Fe_2O_3@CA-01 for Removal of Cr(VI) with Those of Other Iron-Oxide-based Adsorbents

Adsorbent	Q_m (mg/g)	pH	References
PCA	0.64	3	Present study
γ-Fe_2O_3@CA-001	1.14	3	Present study
γ-Fe_2O_3@CA-005	3.94	3	Present study
γ-Fe_2O_3@CA-01	10.2	3	Present study
Commercial α-Fe_2O_3	0.68	3	59
Fe_3O_4@n-SiO_2 nanoparticles	3.78	2	60
Iron oxide nanoparticles embedded in orange peel pith	5.37	1	61
3D flowerlike α-Fe_2O_3	5.4	3	59
Fe_3O_4 (PAA coated and amino functionalized)	11.2	2	62
Diatomite-supported magnetite nanoparticles	11.4	2−2.5	63

DOI: 10.1021/acssuschemeng.5b00384
ACS Sustainable Chem. Eng. 2015, 3, 2142−2152

Fe_2O_3@CA-01. Obviously, the higher content of γ-Fe_2O_3 will lead to stronger Cr(VI) adsorption capacity; besides, the results also reveal that the Cr(VI) adsorption capacity is controllable by adjusting the content of γ-Fe_2O_3 (namely the concentrations of the initial reactants). Moreover, the adsorption capacity of γ-Fe_2O_3@CA-01 is much higher than or comparable with those of other iron-oxide-based adsorbents listed in Table 2, indicating the superior Cr(VI) adsorption capability. Meanwhile, considering the advantages of environmental benefits, facile convenient preparation method, high specific surface area and strong mechanical strength, easy recycle and separation by magnet attraction, and tunability of Cr(VI) adsorption capability, this class of green γ-Fe_2O_3@CA is more favorable and suitable for Cr(VI) removal from contaminated water.

CONCLUSIONS

We demonstrate that the 3D architectures of cellulose aerogels based on the green NaOH/PEG solvent, could be served as suitable template for encapsulating the well-dispersed superparamagnetic γ-Fe_2O_3 nanoparticles via a facile chemical coprecipitation approach. The particle sizes, pore characteristic parameters, magnetic property, and mechanical strength of the synthetic γ-Fe_2O_3@CA could be flexibly tailored by adjusting the total concentration of the $FeCl_3$/$FeSO_4$ salts. Moreover, the composites exhibit superior magnetic responsiveness, which are easily actuated by an applied magnetic field. Meanwhile, the hybrid γ-Fe_2O_3@CA also displays rapid adsorption rate and excellent adsorption ability to remove Cr(VI) heavy metal ions. Therefore, this class of γ-Fe_2O_3@CA is expected to be useful as a kind of novel environmentally friendly magnetically actuated adsorbent for Cr(VI) removal from contaminated water.

ASSOCIATED CONTENT

Supporting Information

The Supporting Information is available free of charge on the ACS Publications website at DOI: 10.1021/acssuschemeng.5b00384.

Data contains XRD and FTIR analysis, thermal treatment (PDF)

Recycling of nanoparticles from black suspension (MPG)

Hydrogel sensitivity to applied magnetic field (MPG)

Adhesion to a magnet surface (MPG)

AUTHOR INFORMATION

Corresponding Author

*J. Li. Tel./fax: +86 45182192399. E-mail: lijiangroup@163.com.

Notes

The authors declare no competing financial interest.

ACKNOWLEDGMENTS

This study was supported by the National Natural Science Foundation of China (grant no. 31270590 and 31470584).

REFERENCES

(1) Laurent, S.; Forge, D.; Port, M.; Roch, A.; Robic, C.; Vander Elst, L.; Muller, R. N. Magnetic iron oxide nanoparticles: synthesis, stabilization, vectorization, physicochemical characterizations, and biological applications. *Chem. Rev.* **2008**, *108*, 2064−2110.

(2) Pouran, S. R.; Raman, A. A. A.; Daud, W. M. A. W. Review on the application of modified iron oxides as heterogeneous catalysts in Fenton reactions. *J. Cleaner Prod.* **2014**, *64*, 24−35.

(3) Urbanova, V.; Magro, M.; Gedanken, A.; Baratella, D.; Vianello, F.; Zboril, R. Nanocrystalline iron oxides, composites, and related materials as a platform for electrochemical, magnetic, and chemical biosensors. *Chem. Mater.* **2014**, *26*, 6653−6673.

(4) Gallo, J.; Kamaly, N.; Lavdas, I.; Stevens, E.; Nguyen, Q. D.; Wylezinska-Arridge, M.; Aboagye, E. O.; Long, N. J. CXCR4−targeted and MMP−responsive iron oxide nanoparticles for enhanced magnetic resonance imaging. *Angew. Chem., Int. Ed.* **2014**, *53*, 9550−9554.

(5) Dhadge, V. L.; Morgado, P. I.; Freitas, F.; Reis, M. A.; Azevedo, A.; Aires-Barros, R.; Roque, A. C. A. An extracellular polymer at the interface of magnetic bioseparations. *J. R. Soc., Interface* **2014**, *11*, 743.

(6) Lin, Y.-S.; Wu, S.-H.; Hung, Y.; Chou, Y.-H.; Chang, C.; Lin, M.-L.; Tsai, C.-P.; Mou, C.-Y. Multifunctional composite nanoparticles: magnetic, luminescent, and mesoporous. *Chem. Mater.* **2006**, *18*, 5170−5172.

(7) Rubio-Retama, J.; Zafeiropoulos, N.; Frick, B.; Seydel, T.; Lopez-Cabarcos, E. Investigation of the relationship between hydrogen bonds and macroscopic properties in hybrid core−shell γ-Fe_2O_3−P(NIPAM-AAS) microgels. *Langmuir* **2010**, *26*, 7101−7106.

(8) Yanik, J.; Uddin, M. A.; Ikeuchi, K.; Sakata, Y. The catalytic effect of red mud on the degradation of poly (vinyl chloride) containing polymer mixture into fuel oil. *Polym. Degrad. Stab.* **2001**, *73*, 335−346.

(9) Xiaotun, Y.; Lingge, X.; Choon, N. S.; Hardy, C. S. O. Magnetic and electrical properties of polypyrrole-coated γ-Fe_2O_3 nanocomposite particles. *Nanotechnology* **2003**, *14*, 624.

(10) Wang, Y.; Teng, X.; Wang, J.-S.; Yang, H. Solvent-free atom transfer radical polymerization in the synthesis of Fe_2O_3@ polystyrene core-shell nanoparticles. *Nano Lett.* **2003**, *3*, 789−793.

(11) Yang, J.; Zhang, H.; Yu, M.; Emmanuelawati, I.; Zou, J.; Yuan, Z.; Yu, C. High−content, well−dispersed γ−Fe_2O_3 nanoparticles encapsulated in macroporous silica with superior arsenic removal performance. *Adv. Funct. Mater.* **2014**, *24*, 1354−1363.

(12) Behrens, S. Preparation of functional magnetic nanocomposites and hybrid materials: recent progress and future directions. *Nanoscale* **2011**, *3*, 877−892.

(13) Guo, Y.; Wang, X.; Sun, R. Cellulose-based self-assembled nanoparticles for antitumor drug delivery. *J. Controlled Release* **2013**, *172*, e85.

(14) Cai, J.; Kimura, S.; Wada, M.; Kuga, S. Nanoporous cellulose as metal nanoparticles support. *Biomacromolecules* **2009**, *10*, 87−94.

(15) Cao, G.; Liu, D. Template-based synthesis of nanorod, nanowire, and nanotube arrays. *Adv. Colloid Interface Sci.* **2008**, *136*, 45−64.

(16) Sun, Z.; Yuan, H.; Liu, Z.; Han, B.; Zhang, X. A highly efficient chemical sensor material for H_2S: α−Fe_2O_3 nanotubes fabricated using carbon nanotube templates. *Adv. Mater.* **2005**, *17*, 2993−2997.

(17) Zhu, X.; Liu, Y.; Zhou, C.; Zhang, S.; Chen, J. Novel and high-performance magnetic carbon composite prepared from waste hydrochar for dye removal. *ACS Sustainable Chem. Eng.* **2014**, *2*, 969−977.

(18) Lian, J.; Duan, X.; Ma, J.; Peng, P.; Kim, T.; Zheng, W. Hematite (α-Fe_2O_3) with various morphologies: ionic liquid-assisted synthesis, formation mechanism, and properties. *ACS Nano* **2009**, *3*, 3749−3761.

(19) Xu, X.; Cao, R.; Jeong, S.; Cho, J. Spindle-like mesoporous α-Fe_2O_3 anode material prepared from MOF template for high-rate lithium batteries. *Nano Lett.* **2012**, *12*, 4988−4991.

(20) Manukyan, K. V.; Chen, Y.-S.; Rouvimov, S.; Li, P.; Li, X.; Dong, S.; Liu, X.; Furdyna, J. K.; Orlov, A.; Bernstein, G. H. Ultrasmall α-Fe_2O_3 superparamagnetic nanoparticles with high magnetization prepared by template-assisted combustion process. *J. Phys. Chem. C* **2014**, *118*, 16264−16271.

(21) Luo, X.; Guo, B.; Luo, J.; Deng, F.; Zhang, S.; Luo, S.; Crittenden, J. Recovery of lithium from wastewater using development of Li ion-imprinted polymers. *ACS Sustainable Chem. Eng.* **2015**, *3*, 460−467.

(22) Liu, X.-M.; Fu, S.-Y.; Xiao, H.-M.; Huang, C.-J. Preparation and characterization of shuttle-like α-Fe2O3 nanoparticles by supermolecular template. *J. Solid State Chem.* **2005**, *178*, 2798−2803.

DOI: 10.1021/acssuschemeng.5b00384
ACS Sustainable Chem. Eng. 2015, 3, 2142−2152

(23) Xiong, R.; Lu, C.; Wang, Y.; Zhou, Z.; Zhang, X. Nanofibrillated cellulose as the support and reductant for the facile synthesis of Fe_3O_4/Ag nanocomposites with catalytic and antibacterial activity. *J. Mater. Chem. A* **2013**, *1*, 14910−14918.
(24) Moon, R. J.; Martini, A.; Nairn, J.; Simonsen, J.; Youngblood, J. Cellulose nanomaterials review: structure, properties and nanocomposites. *Chem. Soc. Rev.* **2011**, *40*, 3941−3994.
(25) Zhang, H.; Wu, J.; Zhang, J.; He, J. 1-Allyl-3-methylimidazolium chloride room temperature ionic liquid: a new and powerful nonderivatizing solvent for cellulose. *Macromolecules* **2005**, *38*, 8272−8277.
(26) Fink, H.-P.; Weigel, P.; Purz, H.; Ganster, J. Structure formation of regenerated cellulose materials from NMMO-solutions. *Prog. Polym. Sci.* **2001**, *26*, 1473−1524.
(27) Wan, C.; Lu, Y.; Jiao, Y.; Cao, J.; Sun, Q.; Li, J. Cellulose aerogels from cellulose−NaOH/PEG solution and comparison with different cellulose contents. *Fibers Polym.* **2015**, *16*, 302−307; *Mater. Sci. Technol.* **2015**, *31*, 1096−1102.
(28) He, J.; Kunitake, T.; Nakao, A. Facile in situ synthesis of noble metal nanoparticles in porous cellulose fibers. *Chem. Mater.* **2003**, *15*, 4401−4406.
(29) Liu, S.; Yan, Q.; Tao, D.; Yu, T.; Liu, X. Highly flexible magnetic composite aerogels prepared by using cellulose nanofibril networks as templates. *Carbohydr. Polym.* **2012**, *89*, 551−557.
(30) Tingaut, P.; Zimmermann, T.; Sèbe, G. Cellulose nanocrystals and microfibrillated cellulose as building blocks for the design of hierarchical functional materials. *J. Mater. Chem.* **2012**, *22*, 20105−20111.
(31) Stagi, L.; De Toro, J. A.; Ardu, A.; Cannas, C.; Casu, A.; Lee, S. S.; Ricci, P. C. Surface effects under visible irradiation and heat treatment on the phase stability of γ-Fe_2O_3 nanoparticles and γ-Fe_2O_3−SiO_2 core−shell nanostructures. *J. Phys. Chem. C* **2014**, *118*, 2857−2866.
(32) Liu, S.; Zhou, J.; Zhang, L. In situ synthesis of plate-like Fe_2O_3 nanoparticles in porous cellulose films with obvious magnetic anisotropy. *Cellulose* **2011**, *18*, 663−673.
(33) Zhu, H.-Y.; Jiang, R.; Xiao, L.; Li, W. A novel magnetically separable-Fe_2O_3/crosslinked chitosan adsorbent: preparation, characterization and adsorption application for removal of hazardous azo dye. *J. Hazard. Mater.* **2010**, *179*, 251−257.
(34) Yin, Y.; Alivisatos, A. P. Colloidal nanocrystal synthesis and the organic−inorganic interface. *Nature* **2005**, *437*, 664−670.
(35) Rudaz, C.; Courson, R.; Bonnet, L.; Calas-Etienne, S.; Sallée, H.; Budtova, T. Aeropectin: fully biomass-based mechanically strong and thermal superinsulating aerogel. *Biomacromolecules* **2014**, *15*, 2188−2195.
(36) Yang, H.; Zhu, W.; Sun, S.; Guo, X. Preparation of monolithic titania aerogels with high surface area by a sol−gel process combined surface modification. *RSC Adv.* **2014**, *4*, 32934−32940.
(37) Jiao, Y.; Wan, C.; Li, J. Room-temperature embedment of anatase titania nanoparticles into porous cellulose aerogels. *Appl. Phys. A: Mater. Sci. Process.* **2015**, *120*, 341−347.
(38) Sescousse, R.; Gavillon, R.; Budtova, T. Aerocellulose from cellulose−ionic liquid solutions: Preparation, properties and comparison with cellulose−NaOH and cellulose−NMMO routes. *Carbohydr. Polym.* **2011**, *83*, 1766−1774.
(39) Olsson, R. T.; Azizi Samir, M. A. S.; Salazar Alvarez, G.; Belova, L.; Strom, V.; Berglund, L. A.; Ikkala, O.; Nogues, J.; Gedde, U. W. Making flexible magnetic aerogels and stiff magnetic nanopaper using cellulose nanofibrils as templates. *Nat. Nanotechnol.* **2010**, *5*, 584−588.
(40) Gawryla, M. D.; van den Berg, O.; Weder, C.; Schiraldi, D. A. Clay aerogel/cellulose whisker nanocomposites: a nanoscale wattle and daub. *J. Mater. Chem.* **2009**, *19*, 2118−2124.
(41) Ouyang, W.; Sun, J.; Memon, J.; Wang, C.; Geng, J.; Huang, Y. Scalable preparation of three-dimensional porous structures of reduced graphene oxide/cellulose composites and their application in supercapacitors. *Carbon* **2013**, *62*, 501−509.
(42) Cai, J.; Liu, S.; Feng, J.; Kimura, S.; Wada, M.; Kuga, S.; Zhang, L. Cellulose−silica nanocomposite aerogels by in situ formation of silica in cellulose gel. *Angew. Chem.* **2012**, *124*, 2118−2121.
(43) Shi, Z.; Gao, H.; Feng, J.; Ding, B.; Cao, X.; Kuga, S.; Wang, Y.; Zhang, L.; Cai, J. In situ synthesis of robust conductive cellulose/polypyrrole composite aerogels and their potential application in nerve regeneration. *Angew. Chem., Int. Ed.* **2014**, *53*, 5380−5384.
(44) Sehaqui, H.; Salajkova, M.; Zhou, Q.; Berglund, L. A. Mechanical performance tailoring of tough ultra-high porosity foams prepared from cellulose I nanofiber suspensions. *Soft Matter* **2010**, *6*, 1824−1832.
(45) Gaudisson, T.; Artus, M.; Acevedo, U.; Herbst, F.; Nowak, S.; Valenzuela, R.; Ammar, S. On the microstructural and magnetic properties of fine-grained $CoFe_2O_4$ ceramics produced by combining polyol process and spark plasma sintering. *J. Magn. Magn. Mater.* **2014**, *370*, 87−95.
(46) Shafi, K. V.; Ulman, A.; Dyal, A.; Yan, X.; Yang, N.-L.; Estournes, C.; Fournes, L.; Wattiaux, A.; White, H.; Rafailovich, M. Magnetic enhancement of γ-Fe_2O_3 nanoparticles by sonochemical coating. *Chem. Mater.* **2002**, *14*, 1778−1787.
(47) Gutfleisch, O.; Willard, M. A.; Brück, E.; Chen, C. H.; Sankar, S.; Liu, J. P. Magnetic materials and devices for the 21st century: stronger, lighter, and more energy efficient. *Adv. Mater.* **2011**, *23*, 821−842.
(48) Zhang, J.; Cao, Y.; Feng, J.; Wu, P. Graphene-oxide-sheet-induced gelation of cellulose and promoted mechanical properties of composite aerogels. *J. Phys. Chem. C* **2012**, *116*, 8063−8068.
(49) Jiang, W.; Pelaez, M.; Dionysiou, D. D.; Entezari, M. H.; Tsoutsou, D.; O'Shea, K. Chromium(VI) removal by maghemite nanoparticles. *Chem. Eng. J.* **2013**, *222*, 527−533.
(50) Unuabonah, E. I.; Günter, C.; Weber, J.; Lubahn, S.; Taubert, A. Hybrid clay: a new highly efficient adsorbent for water treatment. *ACS Sustainable Chem. Eng.* **2013**, *1*, 966−973.
(51) Bhattacharya, A. K.; Naiya, T. K.; Mandal, S. N.; Das, S. K. Adsorption, kinetics and equilibrium studies on removal of Cr(VI) from aqueous solutions using different low-cost adsorbents. *Chem. Eng. J.* **2008**, *137*, 529−541.
(52) Li, J.; Wang, L.; Qi, T.; Zhou, Y.; Liu, C.; Chu, J.; Zhang, Y. Different N-containing functional groups modified mesoporous adsorbents for Cr(VI) sequestration: Synthesis, characterization and comparison. *Microporous Mesoporous Mater.* **2008**, *110*, 442−450.
(53) Khezami, L.; Capart, R. Removal of chromium(VI) from aqueous solution by activated carbons: kinetic and equilibrium studies. *J. Hazard. Mater.* **2005**, *123*, 223−231.
(54) Qiu, B.; Xu, C.; Sun, D.; Yi, H.; Guo, J.; Zhang, X.; Qu, H.; Guerrero, M.; Wang, X.; Noel, N. Polyaniline coated ethyl cellulose with improved hexavalent chromium removal. *ACS Sustainable Chem. Eng.* **2014**, *2*, 2070−2080.
(55) Wang, P.; Lo, I. M. Synthesis of mesoporous magnetic γ-Fe_2O_3 and its application to Cr(VI) removal from contaminated water. *Water Res.* **2009**, *43*, 3727−3734.
(56) Sağ, Y.; Aktay, Y. Kinetic studies on sorption of Cr(VI) and Cu(II) ions by chitin, chitosan and Rhizopus arrhizus. *Biochem. Eng. J.* **2002**, *12*, 143−153.
(57) Miretzky, P.; Cirelli, A. F. Cr(VI) and Cr(III) removal from aqueous solution by raw and modified lignocellulosic materials: A review. *J. Hazard. Mater.* **2010**, *180*, 1−19.
(58) Jia, Z.; Wang, Q.; Ren, D.; Zhu, R. Fabrication of one-dimensional mesoporous α-Fe_2O_3 nanostructure via self-sacrificial template and its enhanced Cr(VI) adsorption capacity. *Appl. Surf. Sci.* **2013**, *264*, 255−260.
(59) Zhong, L. S.; Hu, J. S.; Liang, H. P.; Cao, A. M.; Song, W. G.; Wan, L. J. Self-assembled 3D flowerlike iron oxide nanostructures and their application in water treatment. *Adv. Mater.* **2006**, *18*, 2426−2431.
(60) Srivastava, V.; Sharma, Y. C. Synthesis and Characterization of Fe_3O_4@n-SiO_2 Nanoparticles from an agrowaste material and its application for the removal of Cr(VI) from aqueous solutions. *Water, Air, Soil Pollut.* **2014**, *225*, 1−16.

DOI: 10.1021/acssuschemeng.5b00384
ACS Sustainable Chem. Eng. 2015, 3, 2142−2152

(61) López-Téllez, G.; Barrera-Díaz, C. E.; Balderas-Hernández, P.; Roa-Morales, G.; Bilyeu, B. Removal of hexavalent chromium in aquatic solutions by iron nanoparticles embedded in orange peel pith. *Chem. Eng. J.* **2011**, *173*, 480−485.
(62) Huang, S.-H.; Chen, D.-H. Rapid removal of heavy metal cations and anions from aqueous solutions by an amino-functionalized magnetic nano-adsorbent. *J. Hazard. Mater.* **2009**, *163*, 174−179.
(63) Yuan, P.; Liu, D.; Fan, M.; Yang, D.; Zhu, R.; Ge, F.; Zhu, J.; He, H. Removal of hexavalent chromium [Cr(VI)] from aqueous solutions by the diatomite-supported/unsupported magnetite nanoparticles. *J. Hazard. Mater.* **2010**, *173*, 614−621.
(64) Dupont, L.; Guillon, E. Removal of hexavalent chromium with a lignocellulosic substrate extracted from wheat bran. *Environ. Sci. Technol.* **2003**, *37*, 4235−4241.

DOI: 10.1021/acssuschemeng.5b00384
ACS Sustainable Chem. Eng. 2015, 3, 2142−2152